Flow-Induced Reconfiguration of and Force on Elastic Cantilevers

Jie Wei[1,2] and Jianjun Wu[1,2(✉)]

[1] Key Laboratory of Mechanics on Disaster and Environment in Western China, Attached to the Ministry of Education of China, Lanzhou University, Lanzhou 730000, Gansu, People's Republic of China
wujjun@lzu.edu.cn

[2] College of Civil Engineering and Mechanics, Lanzhou University, Lanzhou 730000, Gansu, People's Republic of China

Abstract. The reconfiguration of elastic beam-like structures (e.g. the foliage) that subjected to cross-flow is widely encountered in nature and engineering applications. Based on a fully coupled numerical algorithm, the fluid–structure interaction between elastic cantilever and cross-flow is investigated in this paper. The immersed boundary-lattice Boltzmann method (IB-LBM) is used to solve the flow involving moving boundaries. The elastic cantilevers are modeled as inextensible Euler-Bernoulli beams and their dynamics are governed by geometrically nonlinear equations. The results suggest that the flow-induced dynamics and fluid forces are sensitive to Cauchy number (Cy). In essence, the flow-induced reconfiguration of elastic cantilevers discussed in this paper is the superposition of large deformation and sustained oscillation. The amplitude as well as the periodicity of drag and lift force are significantly modulated by structure motion. A greater Cy is found to yield a lift force which is comparable with the drag force. The Cauchy-Reconfiguration number curve overall fits the empirical values, in addition to the underestimated values obtained by the present simulations, we attribute it to the streamlined morphology and fluid force in transverse.

Keywords: Reconfiguration · Fluid–structure interactions · Immersed boundary-lattice Boltzmann method · Cauchy number

1 Introduction

The dynamic interactions between fluid flows and flexible structures (FSI) are associate with a broad range of physical process. In nature, the terrestrial/aquatic plants provide important ecosystem services. Due to the flexibility attribute, fluid-structure interaction is ubiquitous for various plant communities and plays a critical role in agriculture and costal protection, involving the lodging of crops and wave attenuation by submerged vegetation [1–3]. For a vegetation canopy, a wave-like motion, which is referred to as *Honami*/*Monami* for terrestrial/aquatic vegetation flow, would be observed when the blades or stalks are forced to bend and vibrate by aero/hydrodynamics loads [4, 5].

X. Zheng and S. Balachandar (Eds.): IUTAM 2023, IUTAM Bookseries 41, pp. 229–249, 2024.
https://doi.org/10.1007/978-3-031-47258-9_15

Such coherent motion is induced by the flexibility attributes of plants and the mixing-layer instability associated with the inflection point of the wind velocity profile [6]. This strong coupling between flow and flexible plants has been confirmed to be correlated with several key scalar transport process, e.g. the dispersion of seeds, spores, and pollens [7, 8]. The fluid-structure interactions are also observed in engineering areas with the increasing broad application of flexible structures. For the sake of flow control, passive slender structures are adopted to augment the wake of bluff bodies [9]. Also, the energy harvesting devices are applied to extract energy from the natural renewable resources (e.g. currents and wind flow) by the special designed flexible oscillating foils [10, 11]. Therefore, with the increasing demands in making precise prediction for both structural dynamics and resistance of the flexible cantilevered structures over a wide range of physical properties and flow conditions, such physical interaction has attracted growing attentions by researchers in the past decade. Moreover, the strong coupling between flexible structures (e.g. flat blades, elastic flags, filaments) and surrounding flows has become a hot and frontier topic in recent interdisciplinary research. Since the relevance in various areas, the related theoretical achievements are crucial to help us comprehend such interactions systematically and design various engineering structures, which take advantage the FSI; on the other hand, predict conditions for structure failure.

Among these FSI cases, the elastic cantilevered structures (e.g. flat plates and filaments) that exposed to cross-flow are widely seen, and the flexibility plays a vital role. With the bending stiffness being overcome by fluid loads, these structures would experience a set of complex dynamics responses, including significant deformations accompanied by large amplitude vibrations [12]. In another way, the flow-driven reconfiguration modulates the surrounding flow and yield a mitigated drag for a structure. Due to this, the risks of failure in uprooting and fracture by surrounding flow are reduced for natural plants. The early efforts, which tried to quantitatively reveal the relation between reconfiguration and drag reduction for vegetation elements, could be dated to Vogel et al. [13, 14]. As is known that, the resistance of rigid bluff bodies varies with stream velocity and follows the classical quadratic scaling law, namely, $F_d \propto U^2$. Yet the variation in resistance versus velocity was found to go more gently for the flexible ones and the Vogel exponent v was introduced to quantify it, which reads as $F_d \propto U^{2+v}$. Since then, the characterization and quantification of the drag scaling law as well as the Vogel exponent have become an open problem. A more comprehensively accepted scope for the Vogel exponent is $-1.3 < v < 0$ and v varies around -0.7, which is summarized from abundant experimental and numerical results, and also coincides with the $v = -2/3$ recovered by dimensional analysis [15, 16]. The dimensional analysis also suggests that Cauchy number (Cy) is the primary parameters in characterizing the coupling system. Remarkably, both the reconfiguration and drag reduction exhibit similar behaviors for those elastic cantilevered specimens with different morphologies, dimensions and flexural rigidity [17, 18]. This suggests that the relation between reconfiguration and drag reduction of these structures with different morphology is similar and controlled by the dimensionless Cy. Following this framework, Cy has been used in the model of flow-flexible vegetation interactions to characterize the impact of reconfiguration on the resistance of an individual vegetation element [19, 20].

Since the recent decade, the interactions between elastic cantilevered structures and flows have been explored with abundant useful insights being gained by studies, especially in establishing the relation between reconfiguration and drag reduction. Nonetheless, further works should be carried out on this issue. On one hand, plenty of experiments have been performed, which verified the results derived from theoretical analysis and also revealed more physical mechanisms. While, in terms of experimental measurements for such FSI system, it is still restrained by the fewer choice of adjustable physical parameters. Some variables, which are associated with the flow conditions and also the structural attribution, are even hard to control. On the other hand, remarkably, the earlier numerical models on flow-induced reconfiguration were simplified. In which, structural motion was confined to static deformation forced by drag and the background flow was reduced to steady state. Thus, some crucial dynamic effects, e.g. the instantaneous, non-uniform distribution structural loads induced by vortex shedding as well as the flow field perturbation from structural vibration were all ignored. However, with the rapid developments in numerical techniques. The FSI numerical methods e.g. Arbitrary Lagrangian-Eulerian Method (ALE), immersed boundary method (IBM) have been confirmed to be capable in fully capturing the coupling between fluid flows and various deformable structures. So far, few numerical attempts have been performed on the elastic cantilevered structure interacts with cross-flow. Therefore, the immersed boundary method is adopted here within the framework of fluid-structure interaction, the present work would focus on the effects of Cauchy number on dynamics behaviours and time-dependent fluid forces of slender elastic cantilevers.

2 Physical Model Statement

In order to emphasize the basic mechanisms of flow-induced dynamics for elastic cantilevers, we consider the structure of length L and is subjected to a uniform incoming flow (see Fig. 1). Available experimental observations suggested that the dynamics of such slender structures were mainly two-dimensional [21]. Thus, following assumptions are made for simplification: (i) The elastic cantilever is inextensible with constant physical attribute of density (ρ_f), elastic modulus (E), width ($w = 0.125L$), thickness ($t = 0.012w$) along the length. (ii) The cantilever only bend in x-y plane without torsion and any out-of-plane deformation. (iii) The 2D background flow is viscous and incompressible. (iv) Gravity and buoyant are disregarded due to structural morphology.

The schematic diagram of physical model is illustrated by Fig. 1. The computational domain is $[-11L, 31L] \times [-11L, 11L]$. The origin of Euler coordinate is fixed at the cantilever's mid-point of initial configuration. The x-axis and y-axis are respectively parallel and normal to the incoming flow.

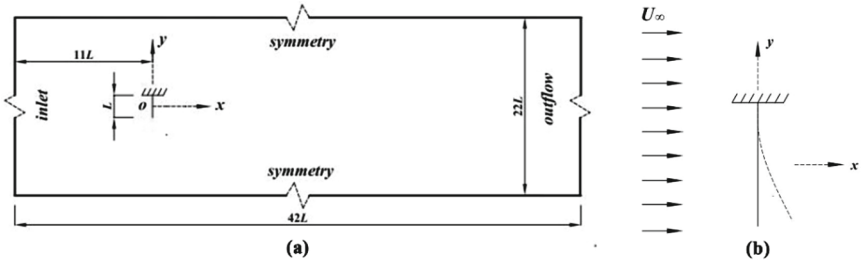

Fig. 1. Schematic of physical model (a). Computational domain; (b). Partial enlarged detail

3 Governing Equations and Numerical Algorithm

Within the framework of IB-LBM, the flow would be solved on fixed Cartesian mesh, while a set of discretized Lagrange grids are used to represent the 1-D elastic cantilever. The effects of structure reconfiguration on the surrounding flow is modeled by a forcing term incorporated into the momentum equations. Thus, the present study implement the FSI simulation by solving the fluid field and structure motion sequentially. Such coupling scheme has been confirmed to be accurate, efficient and robust in papers that involve the similar issue of moving boundary [22–24].

3.1 Mathematical Formulation of Lattice Boltzmann Method for Fluid Flow

As an alternative solver, LBM has been widely adopted by recent papers to solve the flows that governed by N-S equations, especially for the issues involving deformable solid boundaries. Here, the evolution of particle distribution function for the IB-LBM method in single-relaxation form is expressed as follows [25]

$$f_\alpha(\boldsymbol{r}+\boldsymbol{e}_\alpha\delta_t, t+\delta_t) - f_\alpha(\boldsymbol{r}, t) = -\frac{1}{\tau}[f_\alpha(\boldsymbol{r}, t) - f_\alpha^{eq}(\boldsymbol{r}, t)] + \delta t F_\alpha(\boldsymbol{r}, t) \tag{1}$$

$$F_\alpha = (1-\frac{1}{2\tau})\omega_\alpha[\frac{(\boldsymbol{e}_\alpha - \boldsymbol{u})}{c_s^2} + \frac{(\boldsymbol{e}_\alpha \cdot \boldsymbol{u})}{c_s^4}\boldsymbol{e}_\alpha] \cdot \mathbf{f} \tag{2}$$

Equations (1)–(2) include the external forcing term. Through the Chapman–Enskog multi-scale expansion, they can be recovered back to N-S equations. Here, $\boldsymbol{u}$ is the macroscopic velocity, $\mathbf{f}$ is the forcing term. α is the index of discretized velocity space. $\boldsymbol{e}_\alpha$ is the local particle velocity. f_α and f_α^{eq} are the density distribution function and the equilibrium distribution function, respectively. F_α is the forcing term in discretized velocity space. τ is the dimensionless relaxation time and defined as follows

$$\tau = 0.5 + \upsilon / c_s^2 \delta t \tag{3}$$

An incompressible D2Q9 LBGK model [26] is adopted here. It is also denoted as **D2G9**, whose particle velocity set is same with that of the **D2Q9** and the correspondent equilibrium distribution function are given by

$$f_\alpha^{eq} = \begin{cases} -4\sigma \frac{p}{c^2} + s_0(\boldsymbol{u}); \alpha = 0 \\ \lambda \frac{p}{c^2} + s_\alpha(\boldsymbol{u}); \alpha = 1 \sim 4 \\ \gamma \frac{p}{c^2} + s_\alpha(\boldsymbol{u}); \alpha = 5 \sim 8 \end{cases} \tag{4}$$

where, $s_\alpha(\boldsymbol{u}) = \omega_\alpha[\frac{\boldsymbol{e}_\alpha \cdot \boldsymbol{u}}{c_s^2} + \frac{(\boldsymbol{e}_\alpha \cdot \boldsymbol{u})^2}{2c_s^4} - \frac{|\boldsymbol{u}|^2}{2c_s^2}]$, the sound speed $c_s = 1/\sqrt{3}$, the weight coefficients are $\omega_0 = 4/9$, $\omega_{1\text{–}4} = 1/9$, $\omega_{5\text{–}8} = 1/36$ and $\delta = 5/12$, $\lambda = 1/3$, $\gamma = 1/12$. Furthermore, the velocity $\boldsymbol{u}$ and pressure p are computed by following formulas

$$\boldsymbol{u} = (\sum_\alpha f_\alpha \boldsymbol{e}_\alpha)/\rho_f + \delta t \boldsymbol{f}/2 \tag{5}$$

$$p = c_s^2[\sum_{\alpha=1}^{8} f_\alpha + s_0(\boldsymbol{u})]/(1 - \omega_0) \tag{6}$$

3.2 Equations for Structure Dynamics

Within large-deflection regime, the elastic cantilevers are modelled as inextensible Euler-Bernoulli beams, the geometrically nonlinear dynamics equations [27], which is defined in curvilinear coordinate system, and given by

$$\frac{\partial^2 \boldsymbol{X}}{\partial t^2} = \frac{\partial}{\partial s}(T\frac{\partial \boldsymbol{X}}{\partial s}) + \frac{\partial^2}{\partial s^2}(-EI\frac{\partial^2 \boldsymbol{X}}{\partial s^2}) + \boldsymbol{F} \tag{7}$$

the Poisson equation for tension T, which is derived from the inextensibility condition $(\partial \boldsymbol{X}/\partial s)\,(\partial \boldsymbol{X}/\partial s) = 1$, is expressed as

$$\frac{\partial \boldsymbol{X}}{\partial s} \cdot \frac{\partial}{\partial s}(\frac{\partial}{\partial s}(T\frac{\partial \boldsymbol{X}}{\partial s})) = \frac{1}{2}\frac{\partial^2}{\partial t^2}(\frac{\partial \boldsymbol{X}}{\partial s} \cdot \frac{\partial \boldsymbol{X}}{\partial s}) - \frac{\partial^2 \boldsymbol{X}}{\partial t \partial s} \cdot \frac{\partial^2 \boldsymbol{X}}{\partial t \partial s} - \frac{\partial \boldsymbol{X}}{\partial s} \cdot \frac{\partial}{\partial s}(\boldsymbol{F}_b + \boldsymbol{F}) \tag{8}$$

in which, s denotes local coordinates of the Lagrangian points along the length, $\boldsymbol{X} = (X, Y)$ is the Eulerian coordinates of the Lagrange points; $\boldsymbol{F}$ is the external force exerted by the surrounding flow; $\boldsymbol{F}_b$, i.e. the second term on the right-hand side of Eq. (7), is elastic bending force. Equations (7) and (8) are discretized by finite-difference method (FDM) and calculated on staggered grids. More detailed discretization of the governing equations and time marching scheme are described in [28], they would not be covered here.

3.3 Immersed Boundary Method

In this study, the implicit velocity correction-based immersed boundary-lattice Boltzmann method proposed by Wu and Shu (2009) [29] is adopted to solve the flow. As compared to the conventional IB treatments, e.g. the penalty function method [30] and the direct forcing method [31], the forcing terms of this IB scheme are calculated implicitly along with the merits of high computational efficiency and easy implementation. In addition, the non-slip boundary condition could be satisfied precisely without any user-specified parameter. In which, the force density $\mathbf{f}$ is taken as unknown, the velocity $\boldsymbol{u}$ is compartmentalized into the intermediate velocity $\boldsymbol{u}^*$ and the velocity correction $\boldsymbol{\delta u}$, i.e.

$$\boldsymbol{u} = \boldsymbol{u}^* + \boldsymbol{\delta u} \tag{9}$$

According to Eq. (5), they are defined as

$$\boldsymbol{u}^* = (\sum_{\alpha} f_\alpha \boldsymbol{e}_\alpha)/\rho_f \tag{10}$$

$$\boldsymbol{\delta u} = (\delta \mathbf{t}/2\rho_f)\mathbf{f} \tag{11}$$

For a given boundary point $\mathbf{X}_B(s_k)$, the unknown velocity correction $\delta \boldsymbol{u}_B$ is introduced here, $k = 0, 1, \ldots N$. The velocity correction $\boldsymbol{\delta u}$ could be interpolated by

$$\delta \boldsymbol{u}(\boldsymbol{r},t) = \int_\Gamma \delta \boldsymbol{u}_B\left(\mathbf{X}_B^k,t\right)\delta\left(\boldsymbol{r} - \mathbf{X}_B^k(s,t)\right)ds \tag{12}$$

$$\delta\left(\boldsymbol{r} - \mathbf{X}_B^k(s,t)\right) = D_{i,j}^k\left(\boldsymbol{r}_{i,j} - \mathbf{X}_B^k\right) = \frac{1}{\Delta x \Delta y}\delta\left(\frac{x_{i,j} - X_B^k}{\Delta x}\right)\delta\left(\frac{y_{i,j} - Y_B^k}{\Delta y}\right) \tag{13}$$

in which, D is Dirac delta function, and the kernel distribution function as

$$\delta(r) = \begin{cases} (1 + \cos(\pi|r|/2))/4; & |r| < 2 \\ 0; & |r| \geq 2 \end{cases} \tag{14}$$

The following expression of $\boldsymbol{\delta u}$ is obtained by substituting Eq. (13) into Eq. (12)

$$\begin{aligned} \delta \boldsymbol{u}(\boldsymbol{r}_{i,j},t) &= \sum_k \delta \boldsymbol{u}_B(\mathbf{X}_B^k, t) D_{i,j}^k(\boldsymbol{r}_{i,j} - \mathbf{X}_B^k)\Delta s_k \\ &= \sum_k \frac{1}{\Delta x \Delta y}\delta \boldsymbol{u}_B(\mathbf{X}_B^k, t)\delta\left(\frac{x_{i,j} - X_B^k}{\Delta x}\right)\delta\left(\frac{y_{i,j} - Y_B^k}{\Delta y}\right)\Delta s_k \end{aligned} \tag{15}$$

where, velocity of the Lagrangian points $\mathbf{U}_B$, is interpolated by Dirac delta function

$$\mathbf{U}_B(\mathbf{X}_B^k, t) = \sum_{i,j} \boldsymbol{u}(\boldsymbol{r}_{i,j}, t) D_{i,j}^k(\boldsymbol{r}_{i,j} - \mathbf{X}_B^k)\Delta x \Delta y \tag{16}$$

it can be further re-written by substituting Eq. (9) and Eq. (15) into Eq. (16) as follows

$$\begin{aligned}\mathbf{U}_B(\mathbf{X}_B^k, t) &= \sum_{i,j} (\boldsymbol{u}^*(\boldsymbol{r}_{i,j}, t) + \delta\boldsymbol{u}(\boldsymbol{r}_{i,j}, t)) D_{i,j}^k(\boldsymbol{r}_{i,j} - \mathbf{X}_B^k)\Delta x\Delta y \\ &= \sum_{i,j} \boldsymbol{u}^*(\boldsymbol{r}_{i,j}, t) D_{i,j}^k(\boldsymbol{r}_{i,j} - \mathbf{X}_B^k)\Delta x\Delta y \\ &+ \sum_{i,j}\sum_{m} \delta\boldsymbol{u}_B(\mathbf{X}_B^m, t) D_{i,j}^m(\boldsymbol{r}_{i,j} - \mathbf{X}_B^m)\Delta s_m D_{i,j}^k(\boldsymbol{r}_{i,j} - \mathbf{X}_B^k)\Delta x\Delta y\end{aligned} \tag{17}$$

Apparently, Eq. (17) could be written in the form of $[\mathbf{A}]\{\delta\boldsymbol{u}_B\} = \{\mathbf{B}\}$, in which the unknown $\delta\mathbf{u}_B = \{\delta\mathbf{u}_0^B, \delta\mathbf{u}_B^1, \ldots, \delta\mathbf{u}_B^m, \ \ldots \delta\mathbf{u}_B^N\}$. Thus, the velocity correction $\boldsymbol{\delta u}$ could be obtained by substituting the solved $\delta\boldsymbol{u}_B$ into Eq. (12) and the force density $\mathbf{f}$ is also determined by Eq. (11). Furthermore, the fluid load acting on the solid boundary, is

$$\mathrm{f}' = -2\rho_f \delta\boldsymbol{u}_B/\delta t \tag{18}$$

The drag and lift force could be calculated by

$$(F_D, F_L) = \int_\Gamma (f_x', f_y')ds \tag{19}$$

therefore, the drag coefficient and lift coefficient are defined as

$$(Cd, CL) = \frac{(F_D, F_L)}{(1/2)\rho U_\infty^2 L} \tag{20}$$

3.4 Boundary Conditions and Discretization Schemes

For the fluid domain, the uniform velocity incoming flow is imposed on the boundary of $x = -11L$, i.e.

$$u(y) = U_\infty; v = 0 \tag{21}$$

The outflow condition is specified at $x = 31L$, i.e.

$$\partial(u, v, p)/\partial x = 0 \tag{22}$$

On the top and bottom boundary, $y = \pm 11L$, the symmetry condition is specified, i.e.

$$\partial(u, p)/\partial y = 0 \tag{23}$$

The elastic cantilever is treated as moving no-slip wall boundary with its upper point clamped at $\boldsymbol{X}_0(0, 0.5L)$, i.e.

$$\boldsymbol{X} = \boldsymbol{X}_0, \partial\boldsymbol{X}/\partial\boldsymbol{s} = (0, -1) \tag{24}$$

For the free end of a cantilever, the boundary condition is given by

$$\partial^3 \boldsymbol{X}/\partial^3 \boldsymbol{s} = \boldsymbol{0},\ \ \partial^2 \boldsymbol{X}/\partial^2 \boldsymbol{s} = \boldsymbol{0}, T = 0 \tag{25}$$

For the sake of reducing the amount of discretized lattice points and achieving a higher computational efficiency, a non-uniform spatial discretization scheme is employed by this work and the Taylor series least square-based LBM (TLLBM) is adopted to update the particle distribution function. A detailed description for TLLBM could be referred to [32], here it would not be repeat. For the following FSI simulations, uniform grids are generated in the vicinity of the cantilever (a square domain of $[-2L, 2L] \times [-2L, 2L]$) with the minimum mesh size of the computation domain, i.e. $\Delta x_0 = \Delta y_0 = L/80$. While, the mesh size in both x- and y-direction is design to increase gradually in the region away from the cantilever, the maximum mesh size is specified as $\Delta x_{\max} = \Delta y_{\max} = 3.0\Delta x_0$. While, the cantilevers are discretized by uniformly-spaced Lagrangian points along the length, and the structure mesh size is $\Delta s = L/50$.

4 Numerical Results and Discussion

Based on the numerical algorithm described above, the present study implements the FSI simulation by solving Eqs. (1), (2), Eqs. (7), (8) and Eq. (17) sequentially. The FSI simulation code is written by C++ programming language. From Eq. (1), (2), the algorism is discovered to be featured by a good parallelism property. The OpenMP parallelism scheme, therefore, is introduced to decrease the CPU time costs.

4.1 Verification of the Present Numerical Method

Both the treatment on immersed boundary and the numerical solution for structure dynamics that governed by Eqs. (7), (8) are verified as bellow.

For the purpose of giving an assessment for the IB-LBM code on the calculation of flow field, the numerical simulation of flow past a fixed cylinder is performed. It is a classical research in CFD and abundant results are accessible in literatures. The diameter of the circular cylinder is L, the minimum mesh size is set to be $\Delta x_0 = \Delta y_0 = L/80$. Numerical simulations for both the state and unsteady state flow are performed.

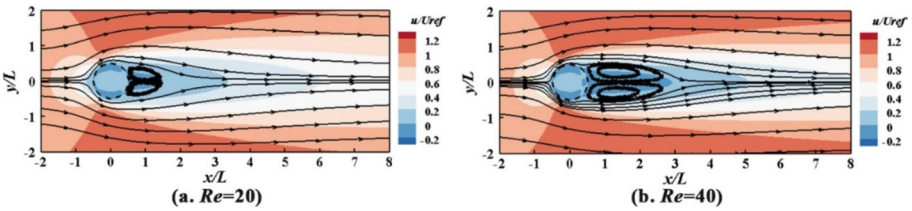

Fig. 2. Velocity Contour and streamlines for flow past a circular cylinder

From Fig. 2, the flow reach the final steady state at $Re = 20$ and 40. A pair of Fopple vortices developed in the wake of the cylinder forming the recirculating region, whose

length increases with *Re*. While, the flow becomes unstable at $Re = 100$. The Fopple vortices shed from the cylinder alternately, forming the kármán vortex street in the wake. The non-dimensional vortex shedding frequency, which is also referred to as the Strouhal number, is $St = f_v L/U$. The time-dependent drag and lift coefficient of the cylinder are defined as Eq. (20) and shown in Fig. 3.

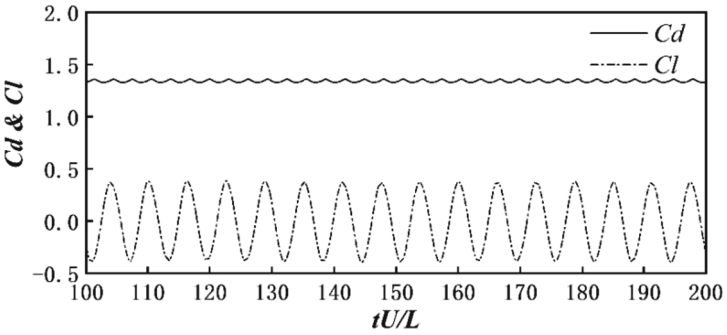

Fig. 3. Evolution of drag and lift coefficient for flow past a circular cylinder at $Re = 100$

Table 1 shows a good coincidence of our data with the data given by the previous literatures. Based on the above analysis, we can conclude that the present numerical algorithm and code are accurate enough to solve flow over bluff body and capable of calculating the fluid loads exerted on the solid-boundary.

Table 1. Drag coefficient, Strouhal number for flow past a cylinder

Case	Reference	*Cd*	*St*
$Re = 20$	Hu et al. [33]	2.21	–
	Niu et al. [34]	2.14	–
	Cui et al. [35]	2.11	–
	Present	2.21	–
$Re = 40$	Kim et al. [36]	1.51	–
	Wu and Shu [29]	1.56	–
	Cui et al. [35]	1.56	–
	Present	1.51	–
$Re = 100$ (time-averaged)	Peng et al. [31]	1.18	0.167
	Wu and Shu [29]	1.33	0.163
	Cui et al. [35]	1.36	0.167
	Present	1.30	0.162

Similarly, the following simulation of a rope-pendulum like motion is carried out to assess the performance of the structural dynamics code segment in the calculation of a forced-vibrating slender beam. The governing equations and boundary conditions are described by Eqs. (7), (8) and Eqs. (24), (25), respectively. The structure is initialized by

$$\boldsymbol{X}(s,0) = (L-s)(\cos\theta, \sin\theta),\ \boldsymbol{X}'(s,0) = (0,0) \tag{26}$$

It would start to swing due to a time-independent force $\boldsymbol{F} = (0, Fy)$. Its length is $L = 1$, the initial angle is $\theta = \pi/10$, the bending rigidity $\gamma = 0.01$ and $Fy = 10$. All of these parameters are identical to that adopted in the study of [28]. The time history of y-displacement of the free-end is plotted in Fig. 4 and agree well with the previous result.

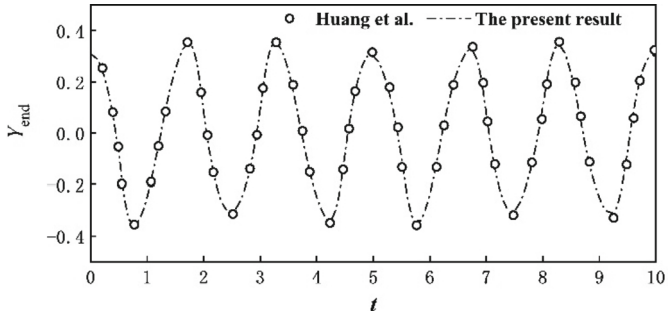

Fig. 4. Time history of y-displacement of free-end

One can conclude from the above facts that both the numerical method and code adopted here are feasible for the further studies in dealing with the flow-structure interactions issue.

4.2 Flow-Induced Reconfiguration and Fluid Forces of Elastic Cantilevers

To systematically explore the interactions between elastic cantilevers and fluid flows, a non-dimensional banding stiffness of flexible structures is introduced, which is defined by Eq. (27) and referred to as Cauchy number (Cy) [2, 16].

$$Cy = Cd_0 \rho_f U^2 A_0 / 2EI \tag{27}$$

in which, Cd_0 and A_0 are the drag coefficient and reference area of an equivalent rigid structure at the same Reynolds number, respectively. EI is the flexural rigidity of an elastic cantilever. In this study, Cy varies within $0.65 \leq Cy \leq 7.20$, while both the Reynolds number and mass ratio are kept and fixed to be $Re = U_\infty L/\nu = 200$, $m^* = 735$. According to the associated literatures, the overall attributes of the coupling system, including the structure vibration and vortex dynamics, are fundamentally similar within a wide range of Re. Therefore, they are confirmed to be relative insensitive to the variation

of Re, especially for $Re > 100$ [37]. Thus, the parameters adopted here are considered to qualify for the target of capturing the rich dynamics features of such FSI system, while at the same time to provide a limitation in computation expense. In following sections, we will focus on the effects of Cy on dynamics behaviors of elastic cantilevers and fluid forces exerted on them.

Effects of Cauchy Number on Flow-Induced Vibration

First, the flow-induced dynamics of elastic cantilevers is investigated in this section. All the FSI calculations are terminated at dimensionless time $t^* = tU/L = 1400$, the time span is sufficient for the coupled fluid-structure system to get the fully developed state.

The time history of non-dimensional displacement component X^* free-end, which is defined as X^* free-end $= X_{\text{free-end}}/L$, is shown in Fig. 5 for 6 selected cases with different Cy.

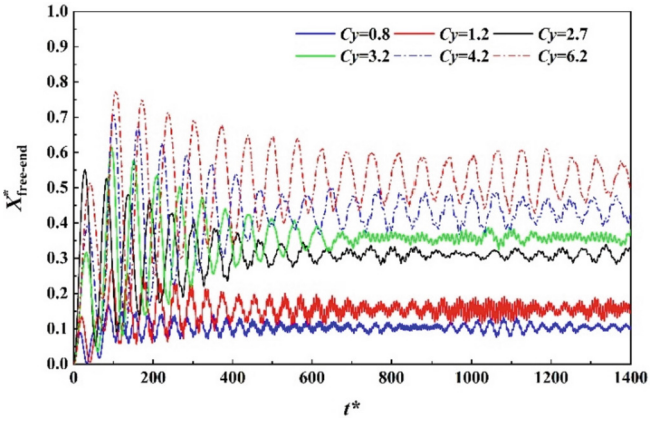

Fig. 5. Time history of free end displacement in x-direction

Clearly that, the dynamics of cantilevers studied here is seen to be featured by vortex-induced vibration (VIV) mode. Moreover, the cantilevers' reconfiguration is featured by large deflection and strongly modulated by Cauchy number. At the onset of reconfiguration, the elastic cantilevers vibrate as the large periodic flapping regime, accompanied by an evident convergence in amplitude. Obviously, an increment in Cy consequent in a increment in vibration period for this regime. For the cases of $Cy < 4.2$, a transition from flapping regime to flutter regime is seen over time, and then the structures vibrate within the small amplitude-high frequency mode. For the flutter regime, the mean deflection decrease for a reduced Cauchy number, also a smaller Cy tends to suppress the amplitude. While, it is interesting to note that the beat vibration is discovered at $Cy = 1.2$. We attribute it to resonance, as the vortex shedding frequency is found to approach the 2-th order structural natural frequency. A detailed spectrum analysis of displacement will be addressed in following sections. In order to give a better visualization for the main signatures of structural motion, the instantaneous configuration of two cantilevers are plotted in Fig. 6.

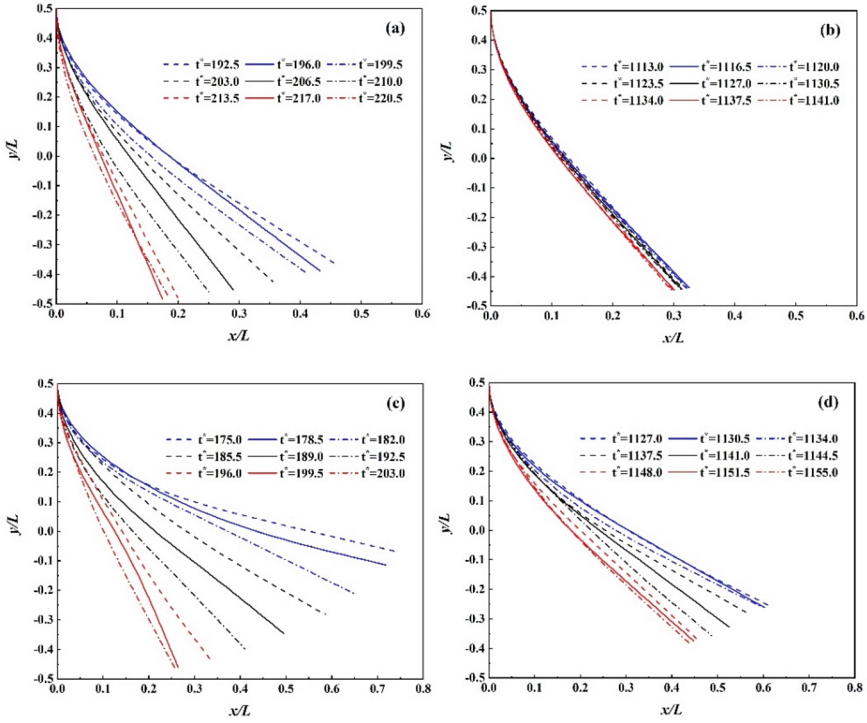

Fig. 6. Instantaneous configuration of the elastic cantilever: (a, b). $Cy = 2.7$; (c, d). $Cy = 6.2$

With the flexural rigidity being overcome by the fluid loads, the elastic cantilevers get aligned with flow through bending and deform to the streamlined morphology, which further result in a reduced frontal area for structures, see Fig. 6. Moreover, the flow-induced reconfiguration of the immersed structures is essentially the superposition of a mean deflection and a sustained oscillation around it. This general trend of structural motion is qualitatively similar to that given by [38, 39]. Figure 6(a, b) present the structural motion within flapping regime and flutter regime during half period of vibration. As the amplitude is far less than the mean deformation, the cantilever is analogous to 'motionless' in Fig. 6(b). While, as shown in Fig. 5 and Fig. 6(c, d), the transition of flapping regime to flutter regime is not observed for $Cy > 4.2$ and the vibration becomes stable with an approximate constant amplitude. Here, we suggest that a threshold value of Cy exists for the coupling system, and if Cy exceeds it, the structural displacement would be fully controlled by flapping. For the present FSI system with $Re = 200$, $m^* = 735$ and aspect ratio $L/t = 2000/3$, the critical Cy is within the range of $3.5 < Cy < 4.2$ and around 4.0. One can also conclude that, for a flow-elastic cantilever system, a greater Cauchy number tends to sustain the flapping regime.

The dynamics of the elastic cantilevers is further explored from the perspective of frequency domain property, the normalized power spectrum density (PSD) of $X^*_{\text{free-end}}(t^*)$ are illustrated by Fig. 7.

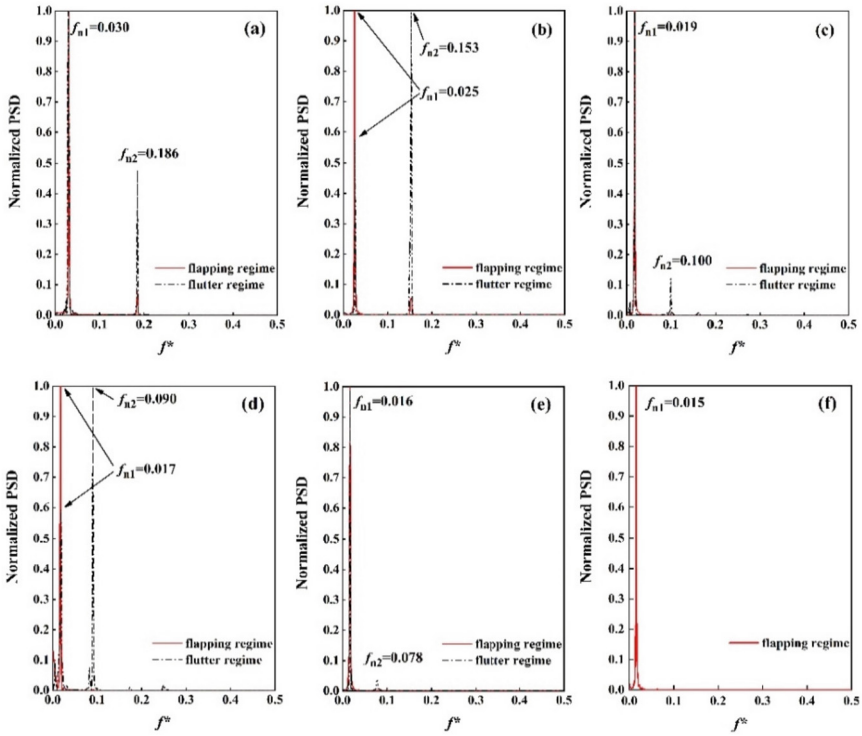

Fig. 7. Normalized power spectrum density of free end displacement in x-direction: (a). $Cy = 0.8$; (b). $Cy = 1.2$; (c). $Cy = 2.7$; (d). $Cy = 3.2$; (e). $Cy = 4.2$; (f). $Cy = 6.2$

At the onset of reconfiguration, the dynamics is featured by flapping and dominated only by the 1-th order natural frequency (f_{n1}). While, the motion is dominated jointly by 1-th and 2-th order natural frequency (f_{n2}) for the subsequent flutter regime. Thus, high frequency oscillation that featured by quasi-periodic is apparent in Fig. 5. It can be inferred from the PSD results that, within large deformation regime, the immersed elastic cantilevers vibrate at the well-defined natural frequency. But it doesn't mean that the effects of the cross-flow, which acts as the excitation source, on dynamics of the elastic cantilevers is absent. As is seen from Fig. 7 (b, d), the dominant frequency is f_{n2} for cantilevers under flutter regime. Here, the ratios of Strouhal number (St) to the 2-th order natural frequency are $St/f_{n2} = 1.03, 1.92$ at $Cy = 1.2$ and 3.2. They are approach to the integer times of f_{n2}, indicating that the impact of f_{n2} on displacement response is amplified by resonance in these cases.

Effects of Cauchy Number on Lift Force and Vortex Shedding

With the increase in Cy, the streamlining becomes more pronounced in cantilevers' morphology. The fluid load component in transverse is thus observed and further forms the lift force. The transverse loads, however, were underemphasized in previous studies. The vortex shedding frequency (f_v), could also be calculated by applying fast Fourier

transform (FFT) on the time series of lift force. Figures 8 and 9 show the evolution of lift coefficient and the corresponding frequency spectrum for the selected cantilevers.

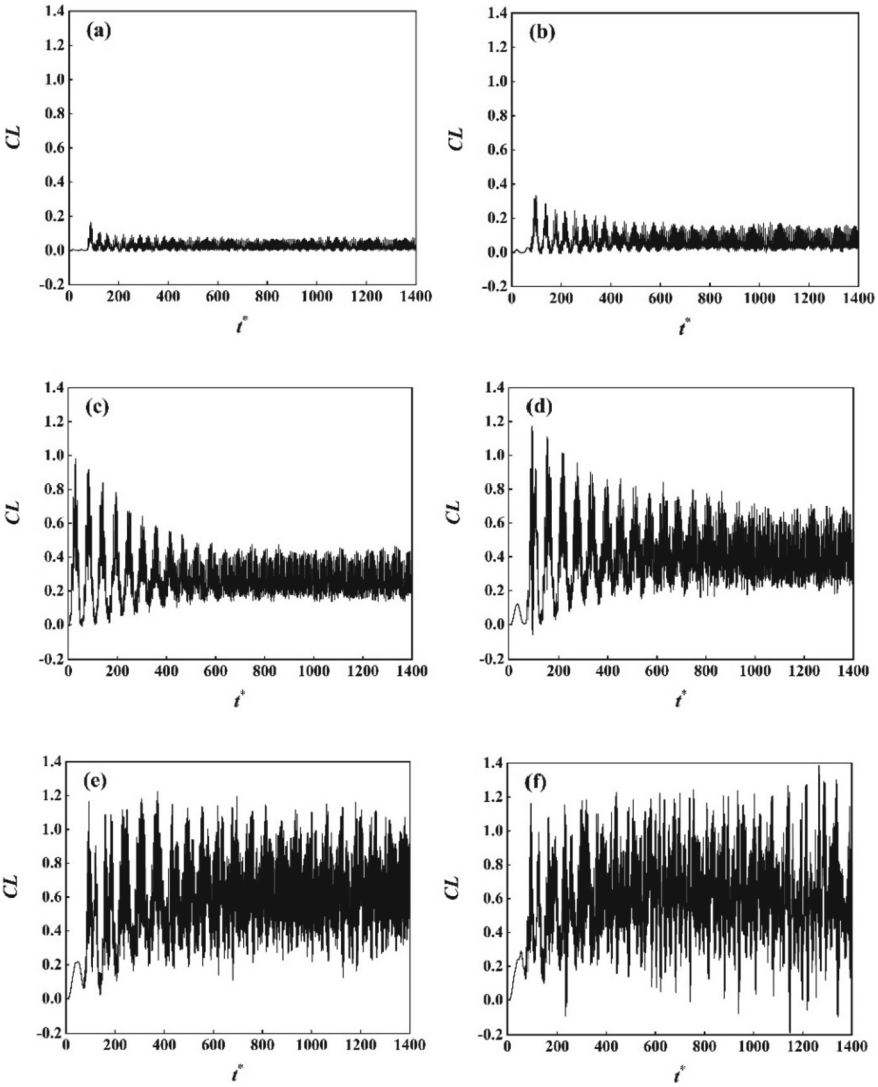

Fig. 8. Time history of lift coefficient for elastic cantilevers with different *Cy*: (a). $Cy = 0.65$; (b). $Cy = 1.2$; (c). $Cy = 2.7$; (d). $Cy = 3.7$; (e). $Cy = 6.2$; (f). $Cy = 7.2$

From Fig. 8, the flow-induced reconfiguration of the examined elastic cantilevers yielded a significant increment in lift coefficient. In terms of amplitude, the transition of structural motion from flapping to flutter is seen to induce an obvious convergence in amplitude of $CL(t^*)$, see Fig. 8(a, d). Note that, at high values of *Cy*, the lift force could be comparable with the stream-wise fluid force, which would be presented in following

section. Furthermore, the time series are characterized by random if Cy exceeds the threshold, see Fig. 8(e, f). Also the isolated and brief snapping events are discovered to be evident, which are associated with the large amplitude flapping motion.

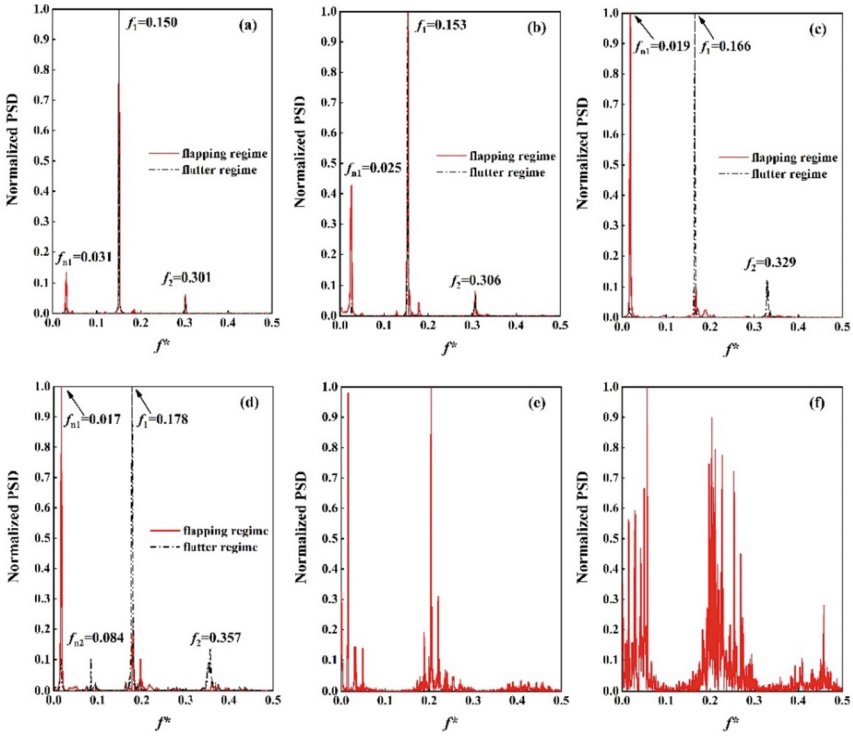

Fig. 9. Normalized power spectrum density of lift coefficient: (a). $Cy = 0.65$; (b). $Cy = 1.2$; (c). $Cy = 2.7$; (d). $Cy = 3.7$; (e). $Cy = 6.2$; (f). $Cy = 7.2$

As is shown in Fig. 9(a, d), four frequency components are evident in the two frequency spectrum plots that are featured by multiple peaks. They are natural frequency f_{n1} and f_{n2}; fundamental frequency f_1 and its harmonic frequency f_2, both of them are associated with Reynolds number and structural geometry. The dimensionless vortex shedding frequency is determined by the dominant frequency, which is treated in the same way to the case of flow past a rigid bluff body. Here, f_1 is identified as the Strouhal number. At $Cy = 0.65$ and 1.2, the dominant frequency is f_1 for both the flapping and flutter regime. With Cy increases, the modulation of frequency f_{n1} on time series $CL(t^*)$, also the vortex shedding, becomes more significantly until f_{n1} supersede f_1 as the dominant frequency within flapping stage, see Fig. 9 (d). While, for flutter regime of structural motion, vibration amplitude is far less than mean deflection; the resulting structural morphology is approximately fixed and the flow is essentially similar to that past a rigid bluff body. Thus, the vortex shedding is dominated by f_1. Furthermore, an evident increment in St for flutter regime could be also seen from Fig. 9(a–d) with the increase in Cy. At relatively high values of Cy (e.g. $Cy = 6.2$ and 7.2), the vibration

mode is maintained to flapping. In addition, the frequency spectrum of time series $CL(t^*)$ manifests as continuous spectrum and presents the typical chaotic feature. Therefore, no definitive peak could be chosen as the dominant frequency.

Effects of Cauchy Number on Drag Force

The effects of Cauchy number on drag force is explored in this section. For the sake of comparison, the drag coefficient (Cd) evolution of the rigid structure is illustrated by Fig. 10(a). At $Cy = 0$, the time series of Cd features by high-frequency fluctuation with the time-averaged value $Cd_{\text{mean}} = 3.20$ when the flow get fully developed.

From Fig. 10, the elastic cantilevers' resistance is also found to be sensitive to Cy. Obviously, the amplitude of drag force as well as the lift force is seen to be strongly correlated to the periodicity and envelope of the structural displacement, especially for flapping regime at onset of the structural reconfiguration, see Fig. 10(c–f). The reconfiguration results in an evident reduction in frontal area. Furthermore, both the streamlined morphology and the resulting reduced frontal area are confirmed to be the two key mechanisms which would result in drag reduction. More visibly in Fig. 10, The mean value of $Cd(t^*)$ gradually decrease with Cy. Here, the Reconfiguration number (R) is introduced to assess the drag reduction quantitatively and defined as

$$R = \frac{F_d}{Cd_0 \rho_f U^2 Lb/2} \tag{28}$$

in which, F_d is the time-averaged drag force exerted on the elastic cantilever, Cd_0 is the drag coefficient of the equivalent rigid specimen [18]. For a rigid body, $R = 1$.

The Cy-R curve is plotted in logarithmic coordinate and illustrated by Fig. 11. It is found that the reconfiguration numbers calculated by this work overall agree with the values given in [15]. All the reconfiguration numbers of the simulated cantilevers are less than 1.0. At small values of Cy, the mean deflection of the given elastic cantilevers is indistinctive, thus the reconfiguration curve is seen to decrease mildly within the range $Cy < 1.0$. In terms of structural resistance, their performance close to the rigid ones. While, for $Cy > 1.0$, the curve starts to decline evidently accompanied by a great slope. The corresponding Vogel exponent is $v = 2\text{d}(\log R)/\text{d}(\log Cy) \approx -0.86$, which falls near the theoretical value of $-2/3$ and within the common accepted range of $v = (-1.2,-0.2)$ [40]. Although the overall tendency of R versus Cy reasonably fits the results that derived from theoretical model, a deviation also exists. Several factors may be responsible for the underestimation of our drag values. (i), it has been shown that the elastic cantilevers become more and more streamlined as Cauchy increases. With the help of the bi-directional coupling mode, the cantilevers' time-dependent configuration could be solved precisely by this work. For the theoretical model proposed in [15], however, the streamlining effects of structures on flow were not introduced. (ii), at greater values of Cy, e.g. Cy > 1, as is seen from above analysis, the fluid force component in transverse is of the same order of the magnitude as drag force. So, it also promote to a more streamlined morphology for cantilevers. This contribution from the transverse fluid loads for deformation, however, was neglected by the theoretical prediction. (iii), the energy exchange between structures and the surrounding flows is omitted by the theoretical model. Through the sustained storage-release of mechanical energy by structures, a

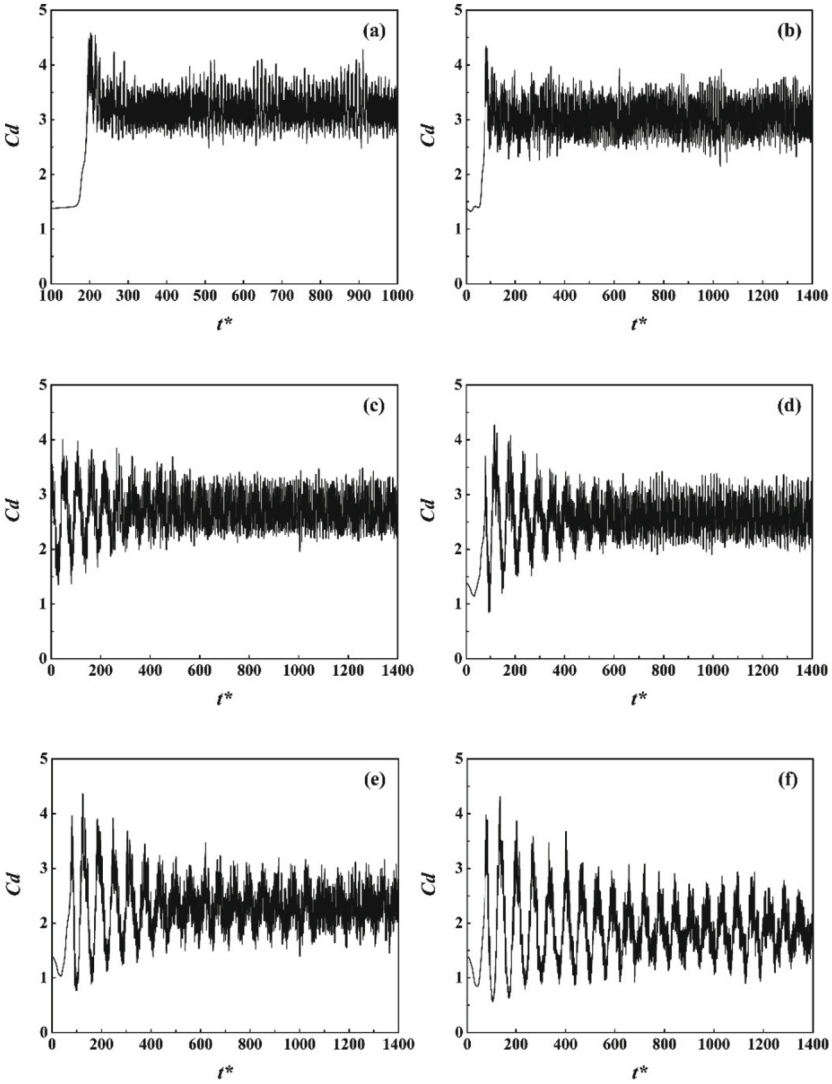

Fig. 10. Time history of drag coefficient for elastic cantilevers with different *Cy*: (a). $Cy = 0$; (b). $Cy = 1.2$; (c). $Cy = 2.7$; (d). $Cy = 3.7$; (e). $Cy = 6.2$; (f). $Cy = 7.2$

smaller drag is needed to maintain the mean deformation. These facts are likely to be responsible for our underestimated value of *R*, especially at $Cy > 1$.

The effects of *Cy* on elastic cantilevers' drag in terms of the frequency domain property are illustrated by Fig. 12. Also, the PSD result of the rigid case is given.

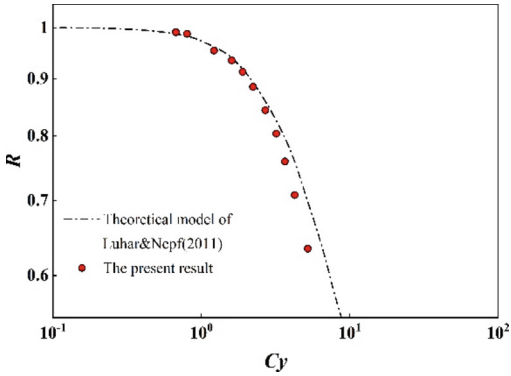

Fig. 11. Reconfiguration number R versus Cauchy number of elastic cantilevers

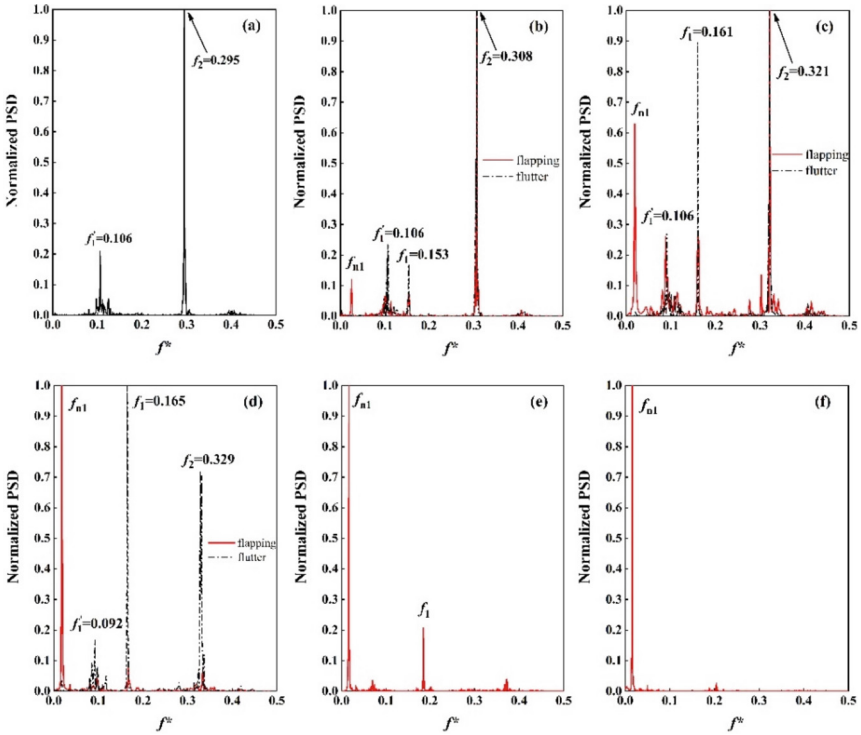

Fig. 12. Normalized power spectrum density of drag coefficient: (a). $Cy = 0$; (b). $Cy = 1.2$; (c). $Cy = 2.2$; (d). $Cy = 2.7$; (e). $Cy = 4.2$; (f). $Cy = 6.2$

In Fig. 12(a), two spectral peaks are apparent, i.e. f**' 1** $= 0.106, f_2 = 0.295$. The ratio of them is an irrational number, indicating that the time series has a typical quasi-periodic feature. Usually, we have the dominant frequency $f_2 = 2f_1 = 2St$ for flow past a bluff body. For elastic cantilevers studied in this paper, multiple peaks appear in the frequency

spectrum of time series $Cd(t^*)$. In addition to f**' 1**and f_2, the frequency f_{n1} and f_1 are also observed. At $Cy = 1.2$ and 2.2, f_2 dominates the fluctuation of $Cd(t^*)$ under both the flapping and flutter regime. The natural frequency f_{n1} shows a growing modulation effect on $Cd(t^*)$ in flapping regime as Cy increases while it is less than the critical value. In Fig. 12(d), f_{n1} supersedes f_2 as the dominant frequency for flapping regime. For flutter regime, on the other hand, as the cantilevers become more streamlined with Cy, a more pronounced modulation effect of f_1 on time series $Cd(t^*)$ is observed until f_1 displace f_2 as the dominant frequency, see Fig. 12(b–d). Moreover, as Cy exceeds the threshold, the structural dynamics would be fully controlled by flapping mode, thus f_{n1} is seen to dominant the fluctuation of time series $Cd(t^*)$, which is in common with the frequency spectra of structure motion.

5 Conclusions

In the framework of the immersed boundary-lattice Boltzmann method, this study focused on the effects of Cauchy number on dynamics behaviors and fluid force exerted on slender elastic cantilevers within $0.65 \leq Cy \leq 7.2$.

In terms of the displacement response, the dynamic reconfiguration of the elastic cantilevers discussed in this paper was mainly characterized by VIV and sensitive to Cy. Two different vibration regimes, namely, flapping and flutter were identified based on the periodicity of vibration. The flow-induced reconfiguration was essentially the superposition of large deformation and sustained vibration. While, a greater Cy yielded an increase in mean deflection for the structures and was found to sustain the flapping regime. In addition, the PSD results revealed that the immersed elastic cantilevers vibrate at the well-defined natural frequency under the large deformation regime.

The strong coupling between dynamic reconfiguration and fluid flow also induced multiple frequency features in fluid forces on the structures. With the increase in Cy, the modulation of natural frequency on both the fluid forces and the vortex shedding process become more significant. Consequently, the amplitude of drag and lift force, as well as the vortex shedding frequency is found to be strongly correlated to the periodicity and the envelope of structural displacement, especially for the flapping regime at the onset of reconfiguration. In transverse, a greater Cy also yielded fluid force component which could not be negligible and its value could be even comparable with the drag force in magnitude. In terms of the drag reduction performance, the time-averaged drag simulated by this study overall agree with the previous results deduced from theoretical model, except for the deviation of underestimation. The streamlined morphology of the structures as well as the transverse fluid load were supposed to be responsible for the deviation.

References

1. Joseph, G., Mohammadi, M., Sterling, M., et al.: Determination of crop dynamic and aerodynamic parameters for lodging prediction. J. Wind Eng. Ind. Aerodyn. **202**, 104169 (2020)

2. Luhar, M., Infantes, E., Nepf, H.: Seagrass blade motion under waves and its impact on wave decay. J. Geophys. Res. Oceans **122**, 3736–3752 (2017)
3. Lei, J., Nepf, H.: Wave damping by flexible vegetation: connecting individual blade dynamics to the meadow scale. Coast. Eng. **147**, 138–148 (2019)
4. Langre, E.D.: Plant vibrations at all scales: a review. J. Exp. Bot. **70**(15), 3521–3531 (2019)
5. Tschisgale, S., Löhrer, B., Meller, R., et al.: Large eddy simulation of the fluid–structure interaction in an abstracted aquatic canopy consisting of flexible blades. J. Fluid Mech. **916**, A43 (2021)
6. Brunet, Y.: Turbulent flow in plant canopies: historical perspective and overview. Bound.-Layer Meteorol. **177**(2–3), 315–364 (2020)
7. Finnigan, J.: Turbulence in plant canopies. Annu. Rev. Fluid Mech. **32**(1), 519–571 (2000)
8. De Langre, E.: Effects of wind on plants. Annu. Rev. Fluid Mech. **40**, 141–168 (2008)
9. O' Connor, J., Revell, A.: Dynamic interactions of multiple wall-mounted flexible flaps. J. Fluid Mech. **870**, 189–216 (2019)
10. Fernandez-Feria, R.: Flutter stability analysis of an elastically supported flexible foil. Application to the energy harvesting of a fully-passive flexible flapping-foil of small amplitude. J. Fluids Struct. **109**, 103454 (2022)
11. Fernandez-Feria, R., Sanmiguel-Rojas, E.: On the feasibility of a flexible foil with passive heave to extract energy from low wind speeds. J. Fluids Struct. **114**, 103751 (2022)
12. Luhar, M., Nepf, H.M.: Wave-induced dynamics of flexible blades. J. Fluids Struct. **61**, 20–41 (2016)
13. Vogel, S.: Drag and flexibility in sessile organisms. Am. Zool. **24**(1), 37–44 (1984)
14. Vogel, S.: Drag and reconfiguration of broad leaves in high winds. J. Exp. Bot. **40**(8), 941–948 (1989)
15. Luhar, M., Nepf, H.M.: Flow-induced reconfiguration of buoyant and flexible aquatic vegetation. Limnol. Oceanogr. **56**(6), 2003–2017 (2011)
16. Leclercq, T., de Langre, E.: Drag reduction by elastic reconfiguration of non-uniform beams in non-uniform flows. J. Fluids Struct. **60**, 114–129 (2016)
17. Gosselin, F., De Langre, E., Machado-Almeida, B.A.: Drag reduction of flexible plates by reconfiguration. J. Fluid Mech. **650**, 319–341 (2010)
18. Gosselin, F.P., De Langre, E.: Drag reduction by reconfiguration of a poroelastic system. J. Fluids Struct. **27**(7), 1111–1123 (2011)
19. Beudin, A., Kalra, T.S., Ganju, N.K., et al.: Development of a coupled wave-flow-vegetation interaction model. Comput. Geosci. **100**, 76–86 (2017)
20. Lu, J., Dai, H.C.: Numerical modeling of pollution transport in flexible vegetation. Appl. Math. Model. **64**, 93–105 (2018)
21. Schouveiler, L., Eloy, C., Le Gal, P.: Flow-induced vibrations of high mass ratio flexible filaments freely hanging in a flow. Phys. Fluids **17**(4), 047104 (2005)
22. Revell, A., Mandal, P., Day, P.: Application of a lattice Boltzmann-immersed boundary method for fluid-filament dynamics and flow sensing. J. Biomech. **49**(11), 2143–2151 (2016)
23. Kanchan, M., Maniyeri, R.: Numerical simulation of buckling and asymmetric behavior of flexible filament using temporal second-order immersed boundary method. Int. J. Numer. Meth. Heat Fluid Flow **30**(3), 1047–1095 (2020)
24. Wu, J., Cheng, Y., Zhang, C., et al.: Simulating vortex induced vibration of an impulsively started flexible filament by an implicit IB–LB coupling scheme. Comput. Math. Appl. **79**(1), 159–173 (2020)
25. Guo, Z., Zheng, C., Shi, B.: Discrete lattice effects on the forcing term in the lattice Boltzmann method. Phys. Rev. E **65**(4), 046308 (2002)
26. Guo, Z., Shi, B., Wang, N.: Lattice BGK model for incompressible Navier-Stokes equation. J. Comput. Phys. **165**(1), 288–306 (2000)

27. He, S., Liu, H., Shen, L.: Simulation-based study of turbulent aquatic canopy flows with flexible stems. J. Fluid Mech. **947**, A33 (2022)
28. Huang, W.X., Shin, S.J., Sung, H.J.: Simulation of flexible filaments in a uniform flow by the immersed boundary method. J. Comput. Phys. **226**(2), 2206–2228 (2007)
29. Wu, J., Shu, C.: Implicit velocity correction-based immersed boundary-lattice Boltzmann method and its applications. J. Comput. Phys. **228**, 1963–1979 (2009)
30. Feng, Z.G., Michaelides, E.E.: The immersed boundary-lattice Boltzmann method for solving fluid-particles interaction problems. J. Comput. Phys. **195**, 602–628 (2004)
31. Fadlun, E.A., Verzicco, R., Orlandi, P., et al.: Combined immersed-boundary finite-difference methods for three dimensional complex flow simulations. J. Comput. Phys. **161**, 35–60 (2000)
32. Shu, C., Niu, X.D., Chew, Y.T.: Taylor-series expansion and least-squares-based lattice Boltzmann method: two-dimensional formulation and its applications. Int. J. Mod. Phys. C **14**(07), 925–944 (2003)
33. Hu, Y., Yuan, H., Shu, S., et al.: An improved momentum exchanged-based immersed boundary–lattice Boltzmann method by using an iterative technique. Comput. Math. Appl. **68**, 140–155 (2014)
34. Niu, X.D., Shu, C., Chew, Y.T., et al.: A momentum exchange-based immersed boundary-lattice Boltzmann method for simulating incompressible viscous flows. Phys. Lett. A **354**, 173–182 (2006)
35. Cui, X.W., Yao, X.L., Wang, Z.K., et al.: A hybrid wavelet-based adaptive immersed boundary finite-difference lattice Boltzmann method for two-dimensional fluid–structure interaction. J. Comput. Phys. **333**, 24–48 (2017)
36. Kim, J., Kim, D., Choi, H.: An immersed-boundary finite-volume method for simulations of flow in complex geometries. J. Comput. Phys. **171**, 132–150 (2001)
37. Mazharmanesh, S., Young, J., Tian, F.B., et al.: Energy harvesting of inverted piezoelectric flags in an oscillating flow. J. Fluids Struct. **115**, 103762 (2022)
38. Zhang, X., He, G., Zhang, X.: Fluid–structure interactions of single and dual wall-mounted 2D flexible filaments in a laminar boundary layer. J. Fluids Struct. **92**, 102787 (2020)
39. Silva-Leon, J., Cioncolini, A., Filippone, A., et al.: Flow-induced motions of flexible filaments hanging in cross-flow. Exp. Thermal Fluid Sci. **97**, 254–269 (2018)
40. Henriquez, S., Barrero-Gil, A.: Reconfiguration of flexible plates in sheared flow. Mech. Res. Commun. **62**(1), 1–4 (2014)